Grafting Porphyrins (Face-to-Edge/Orthogonal versus Face-to-Face/Parallel) to ZnO en Route toward Dye-Sensitized Solar Cells†

Fabian Werner,[‡,▽] Jan-Frederik Gnichwitz,[‡,§,▽] Renata Marczak,[⊥,▽] Emilio Palomares,[#,¶,▽] Wolfgang Peukert,[*,⊥,▽] Andreas Hirsch,[*,‡,§,▽] and Dirk M. Guldi[*,‡]

Department of Chemistry and Pharmacy, Friedrich-Alexander-University Erlangen−Nuremberg, Egerlandstrasse 3, 91058 Erlangen, Germany, Interdisciplinary Center of Molecular Materials (ICMM), Friedrich-Alexander-University Erlangen−Nuremberg, Henkestrasse 42, 91054 Erlangen, Germany, Institute of Particle Technology, Friedrich-Alexander-University Erlangen−Nuremberg, Cauerstrasse 4, 91058 Erlangen, Germany, Institute of Chemical Research of Catalonia (ICIQ), Avda. Països Catalans 16, E-43007 Tarragona, Spain, and Institució Catalana de Recerca i Estudis Avançats (ICREA), Avda. Lluïs Companys 23, E-08010 Barcelona, Spain

Received: March 26, 2010; Revised Manuscript Received: June 4, 2010

Novel types of binding motives have been investigated within the context of sensitizing ZnO-based dye-sensitized solar cells with metalloporphyrins. In particular, a complementary class of metalloporphyrin has been synthesized to probe the impact of a face-to-edge/orthogonal versus face-to-face/parallel orientation of the metalloporphyrin with respect to ZnO and has been compared to TiO_2-based dye-sensitized solar cells. Our studies provide a deep and detailed understanding of the individual electron-transfer processes at the ZnO/metalloporphyrin interface, that is, electron injection, recombination, and dye regeneration, by means of steady-state and time-resolved techniques. Interestingly, we found that for our novel ZnO/metalloporphyrin systems, the injection efficiencies are close to unity, despite their long, nonconjugated anchoring group length.

Introduction

Direct wide band gap semiconductors like zinc oxide (ZnO) (i.e., $E_g > 3.3$ eV) with comparatively large exciton binding energies (i.e., > 60 meV) are interesting materials. To this end, nanostructured ZnO materials, owing to their high electron mobility and their nontoxicity, have emerged as an intriguing alternative to titanium dioxide (titania, TiO_2) for the use in solar energy conversion schemes.[1] Easily accessible and controllable structures (down to the nanometer regime) of ZnO have led to nanocombs, nanorings, nanohelixes/nanosprings, nanobelts, nanowires, and nanocages.[2−7] These unique nanostructures unambiguously demonstrate that ZnO probably has the richest family of nanostructures among all materials, both in structures and in properties. In fact, it opens the possibility of effectively engineering electron pathways and surfaces for dye adsorption. In this context, the longer electron mean-free path in nanostructured ZnO materials is a key asset in allowing for thicker device design without compromising the overall electron collection. Equally important is the observation that the trap density in ZnO is lower than that in TiO_2. As a direct consequence of the latter, the minority carrier diffusion length and lifetimes in bulk n-type ZnO are longer than those in n-type TiO_2.[8,9]

Dye-sensitized solar cells (DSSCs) with low cost, easy fabrication, and relatively high solar-to-electricity conversion efficiency have emerged as an important photovoltaic technology.[10−12] However, further improvements in the efficiency and stability, namely, minimizing loss mechanisms and improving light harvesting, depend critically on component materials, structures, and processing techniques.[13] To name a few, factors playing a role are particle size and shape, porosity, necking structure, film thickness, distance between electrodes, electrolyte composition, dye anchoring, and dye structure. For DSSCs that are based on n-type ZnO, the instability/lability when anchoring the commonly used carboxylate anchoring groups adds another difficulty.[14]

Porphyrins, on the other hand, with their rich and extensive absorptions throughout the visible region of the solar spectrum, hold particularly great promise as integrative dyes/sensitizers with increased absorptive cross sections/light-harvesting features.[15] Their high electronic excitation energy, typically exceeding 2.0 eV, powers a strongly exergonic electron transfer and intercedes hereby the conversion between light and chemical/electrical energy. Another important feature of these dyes/sensitizers is their highly delocalized π-electron system. Rich redox properties render porphyrins as essential components in important biological electron-transport systems including photosynthesis and respiration.[16] Notable is the fact that promising results have already been reported upon implementing porphyrins into conventional TiO_2-based solar cells.[17−20] In this regard, the most efficient systems rely on porphyrins equipped with anchoring groups that are directly attached to their pyrrolic rings or via a conjugated linker to those. A functionalization of the porphyrin core can influence the redox chemistry of the porphyrins. Therefore, porphyrins that were synthetically altered at the phenyl groups of tetra-phenyl porphyrins leave the porphyrin core unchanged and have less influence on the redox chemistry. In the current work, these porphyrins are discussed in conjunction with ZnO.

† Part of the "Michael R. Wasielewski Festschrift".

* To whom correspondence should be addressed. Phone: +49 9131 8527341. Fax: +49 9131 85-28307. E-mail: guldi@chemie.uni-erlangen.de.

‡ Department of Chemistry and Pharmacy, Friedrich-Alexander-University Erlangen−Nuremberg.

§ Interdisciplinary Center of Molecular Materials (ICMM), Friedrich-Alexander-University Erlangen−Nuremberg.

⊥ Institute of Particle Technology, Friedrich-Alexander-University Erlangen−Nuremberg.

Institute of Chemical Research of Catalonia (ICIQ).

¶ Institució Catalana de Recerca i Estudis Avançats (ICREA).

▽ E-mail: fabian.werner@chemie.uni-erlangen (F.W.); jan-frederik.gnichwitz@chemie.uni-erlangen (J.-F.G.); R.Marczak@lfg.uni-erlangen (R.M.); epalomares@iciq.es (E.P.); andreas.hirsch@chemie.uni-erlangen (A.H.); W.Peukert@lfg.uni-erlangen (W.P.).

10.1021/jp102737a © XXXX American Chemical Society

SCHEME 1: (a) Face-to-Edge/Orthogonal and (a) Face-to-Face/Parallel Orientations of Linking Porphyrins As Dyes/ Sensitizers to Nanostructured Oxides

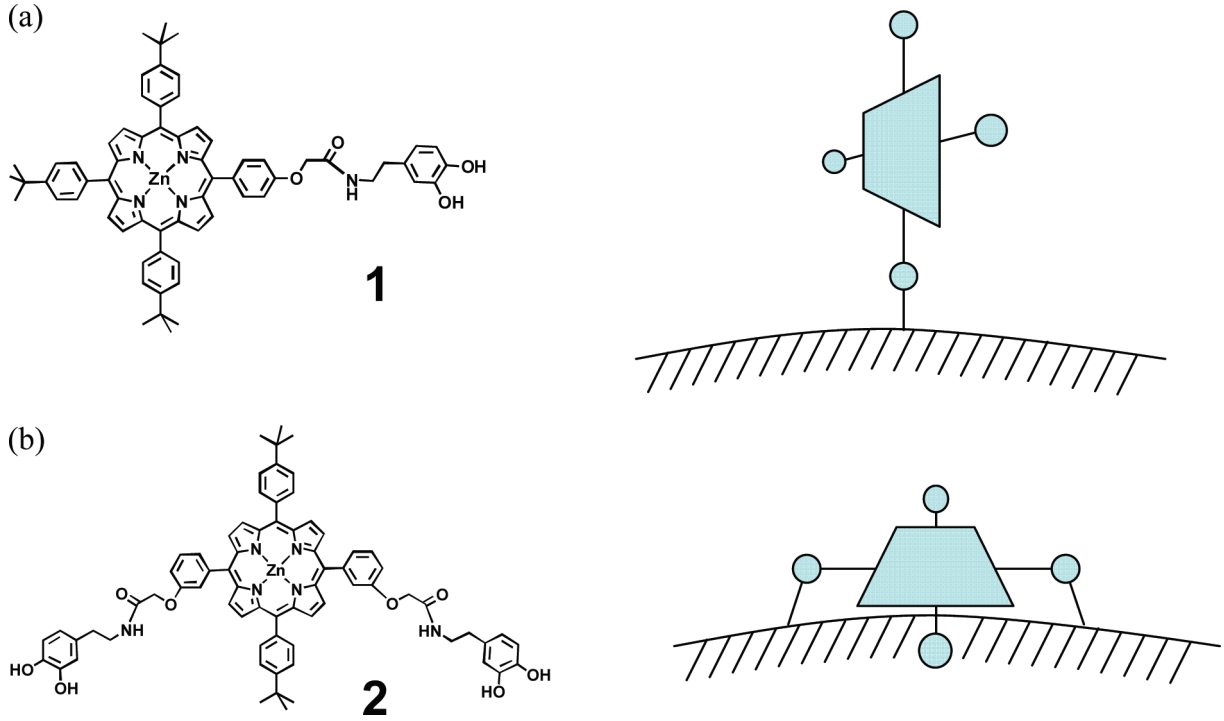

SCHEME 2: Synthesis of 5,15-(*N*-(3,4-Dihydroxyphenethyl)-2-phenoxyacetamide)-10,20-(*p-tert*-butyltriphenyl)porphyrinato-zinc (2)

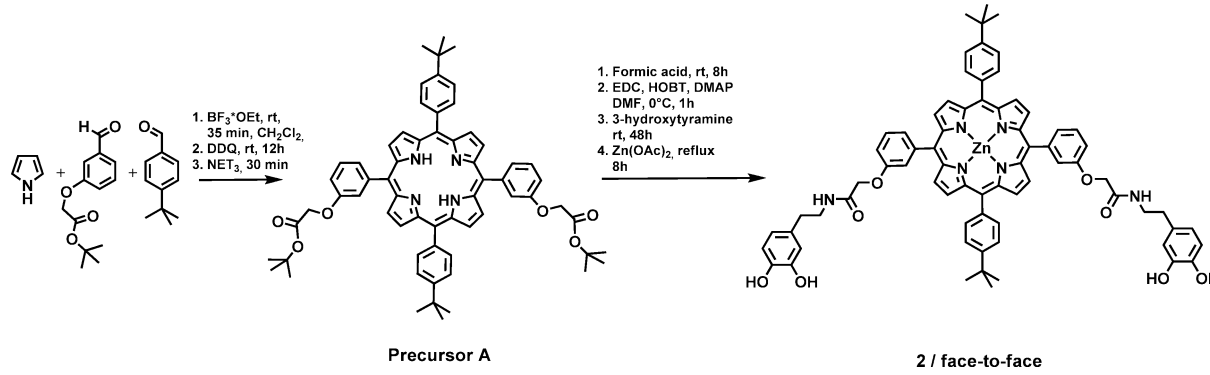

Linking porphyrins as dyes/sensitizers to ZnO necessitates the identification of an appropriate chemical functionality that guarantees the control over the hierarchy and structure of ZnO/porphyrin nanohybrids. Importantly, the charge-transfer efficiency at the semiconductor/dye interface depends, among numerous other factors, on the way that the chromophore is attached.[21−23] For instance, a "multipodal" linker offers unique control over the orientation and distance of the dye/sensitizer at the metal oxide surface.[24−26] Likewise, a face-to-face/parallel rather than a face-to-edge/orthogonal orientation seems to be responsible for as much as a 5-fold increase in the short circuit photocurrent (I_{sc}) and results in the significantly changed open circuit photovoltage (V_{oc}).[27]

In this context, deprotonated catecholates represent a promising class of functional groups that facilitate the binding of, for example, porphyrins to ZnO through the formation of five-membered chelate rings.[2,28,29] Yet, the interactions of such catecholate-appended porphyrins with ZnO have not been fully investigated. Notable is also that ZnO is biosafe and biocompatible.

This is where the current investigation was expected to make a significant contribution. In particular, we have addressed aspects that relate to the use of catecholates as a powerful means to bind porphyrins to films of nanostructured ZnO materials and to their photovoltaic applications by shedding light onto key features such as kinetics of charge injection, charge recombination, charge regeneration, and so forth. In addition, the relative ZnO/porphyrin orientation, that is, face-to-edge/orthogonal versus face-to-face/parallel (see Scheme 1), was varied by altering the functionalization of the porphyrin to elucidate the influence thereof. Specifically, **1** featured a single anchoring group in the para position of one phenyl ring, and **2**, having two anchoring groups, both in meta position of the translocated phenyl rings of the porphyrin, was newly synthesized.

Experimental Section

Synthesis of the Dye Molecules. An overview of the synthesis is depicted in Scheme 2. All chemicals were purchased by chemical suppliers and used without further purification. All analytical reagent-grade solvents were purified by distillation. Dry solvents were prepared using customary literature procedures.[30] For thin-layer chromatography (TLC), Riedel-de Haën silica gel F254 and Merck silica gel 60 F254 were used. Detection was accomplished with an UV lamp and iodine chamber. Flash chromatography (FC) utilized Merck silica gel

60 (230−400 mesh, 0.04−0.063 nm). Solvents were purified by distillation prior to use. For UV−Vis spectroscopy, a Shimadzu UV-3102 PC UV/Vis/NIR scanning spectrophotometer was used; absorption maxima λ_{max} are given in nm. Mass spectrometry utilized an AXIMA Confidence MALDI TOF mass spectrometer, nitrogen UV laser, 50 Hz, λ = 337 nm wavelength, Shimadzu. 2-[(2*E*)-3-(4-*tert*-Butylphenyl)-2-methylprop-2-enylidene] malononitrile (DCTB) and 2,5-dihydroxybenzoicacid (DHB) were used as the matrix. For NMR spectroscopy, a JEOL JNM EX 400 and JEOL JNM GX 400 and Bruker Avance 300 were used. The chemical shifts are given in ppm relative to tetramethylsilane (TMS). The resonance multiplicities are indicated as s (singlet), d (doublet), t (triplet), q (quartet), quin (quintet), and m (multiplet), and nonresolved and broad resonances are indicated as br. Elemental analysis (C, H, N) succeeded by combustion and gas chromatographical analysis with an EA 1110 CHNS analyzer (CE Instruments).

5,15-(*m*-*tert*-Butylacetatophenoxy)-10,20-(*p*-*tert*-butylphenyl)porphyrin (A). A solution of 6.8 mL of pyrrole (0.10 mol), 8.37 mL of 4-*tert*-butylbenzaldehyde (0.05 mol), 11.8 g *tert*-butyl 2-(3-formylphenoxy)acetate (0.05 mol), 20 mL of ethanol, and 100 mg of tetraphenyl phosphonium chloride dissolved in 2.5 L of dichloromethane was stirred for 15 min. Then 6.3 mL of boron trifluoride etherate (0.049 mol) was added, changing the color of the solution to purple−red. Next, the mixture was stirred for at least 35 min but not longer than 40 min. Further, 16.69 g of 2,3-dichloro-5,6-dicyano-1,4-benzoquinone (DDQ, 0.075 mol) was added under ambient conditions. The reaction mixture was stirred for 15 h followed by neutralization with 10 mL of triethylamine. The solvent was removed via evaporation and filtered over silica in dichloromethane. The residue was purified via repeated column chromatography using dichloromethane as the eluent. The product was obtained by crystallization in pentane. The yield was 400 mg (2.1%).

^{1}H NMR ($CDCl_3$, 400 MHz, RT): δ [ppm] = −2.80 (s, 2H), 1.44 (s, 18H), 1.62 (s, 18H), 4.70 (s, 4H), 7.36 (dd, ^4J = 2.5 Hz, ^3J = 8.3 Hz, 2H), 7.65 (m, 2H), 7.77 (m, 6H), 7.86 (d,^3J = 7.3 Hz, 2H), 8.14 (d,^3J = 8.2 Hz, 4H), 8.86 (d,^3J = 4.7 Hz, 4H), 8.88 (d,^3J = 4.7 Hz, 4H). ^{13}C NMR ($CDCl_3$,100.5 MHz, RT): δ [ppm] = 27.9, 31.6, 34.8, 65.7, 76.6, 82.4, 114.5, 119.4, 120.4, 120.8, 123.6, 127.6, 128.4, 134.5, 139.1, 143.6, 150.6, 156.3, 168.1. EA: calculated for $C_{64}H_{66}N_4O_6 \cdot 2H_2O$ (1023): C, 75.12; H, 6.90; N, 5.48; found: C, 74.75; H, 6.50; N, 5.45. MS (MALDI, DHB): *m*/*z*: 986 $[M]^+$.

5,15-(*N*-(3,4-Dihydroxyphenethyl)-2-phenoxyacetamide)-10,20-(*p*-*tert*-butylphenyl)porphyrin (B). A solution containing 400 mg of porphyrin **A** (0.41 mmol) and 200 mL formic acid was stirred overnight to obtain the deprotected acid. Progress of the reaction was followed via TLC. After completion, the solvent was removed in a rotary evaporator and the residue transferred to toluene and evaporated twice to remove any residual formic acid. The product was finally dried under vacuum. The dried product was dissolved in dimethylformamide at 0 °C. Then, 252 mg of 1-ethyl-3-(3-dimethylaminopropyl)-carbodiimide hydrochloride (1.32 mmol), 177 mg of 1-hydroxybenzotriazole (1.32 mmol), and 160 mg of 4-(dimethylamino)pyridine (1.32 mmol) were added, and the solution was stirred for 1 h at 0 °C. After that period, 250 mg of 3-hydroxytyramine hydrochloride (1.32 mmol) was added to the solution, and the mixture was stirred at room temperature for 48 h. The solvent was removed on a rotary evaporator, and the residue was purified via column chromatography on silica gel with a mixture of dichloromethane/methanol (19:1) as the eluent to afford 260 mg of the product. Yield: 45%.

^{1}H NMR (400 MHz, 25 °C, THF-d^8): δ [ppm] = −2.71 (s, 2H), 1.60 (s, 18H), 2.64 (t, ^3J = 7.3 Hz, 4H), 3.53 (dd, ^3J = 6.7 Hz, ^3J = 14.0 Hz, 4H), 4.64 (s, 4H), 6.44 (dd, ^4J = 2.1 Hz, ^3J = 7.9 Hz, 2H), 6.57 (d, ^3J = 7.9 Hz, 2H), 6.71 (d, ^4J = 1.6 Hz, 2H), 7.40 (dd, ^4J = 2.4 Hz, ^3J = 8.3 Hz, 2H), 7.55 (t, ^3J = 5.6 Hz, 4H), 7.68 (m, 4H), 7.83 (m, 10H), 8.11 (d,^3J = 8.1 Hz, 4H), 8.85 (m, 8H).^{13}C NMR (100.5 MHz, 25 °C, THF-d^8): δ [ppm] = 31.9, 35.3, 35.8, 41.3, 68.4, 114.7, 115.7, 116.2, 120.0, 120.3, 120.9, 122.3, 124.3, 128.3, 129.1, 131.1, 135.1, 139.8, 144.4, 144.5, 145.9, 151.2, 157.1, 162.8, 168.5. EA: calculated for $C_{72}H_{68}N_6O_8 \cdot CH_2Cl_2 \cdot 4\ H_2O$ (1302): C, 67.32; H, 6.04; N, 6.45; found: C, 67.48; H, 6.28; N, 6.28. MS (MALDI, DCTB): *m*/*z*: 1147 $[M]^+$.

5,15-(*N*-(3,4-Dihydroxyphenethyl)-2-phenoxyacetamide)-10,20-(*p*-*tert*-butyltriphenyl)porphyrinato-zinc (2). An amount of 200 mg of porphyrin **B** (0.17 mmol) was dissolved in 200 mL of THF, and 80 mg of zinc acetate (0.44 mmol) was added. The mixture was heated to reflux over a period of 8 h. The reaction was monitored by TLC until the disappearance of the free base porphyrin was observed. The solution was concentrated on a rotary evaporator, precipitated with water, and finally filtered. The dried product was obtained as a purple−red solid in very good yield (200 mg, 98%).

^{1}H NMR (400 MHz, 25 °C, THF-d^8): δ [ppm] = 1.62 (s, 18H), 2.63 (t, ^3J = 7.3 Hz, 4H), 3.40 (dd, ^3J = 6.7 Hz, ^3J = 14.2 Hz, 4H), 4.63 (s, 4H), 6.44 (dd, ^4J = 2.1 Hz, ^3J = 7.9 Hz, 2H), 6.58 (m, 4H), 7.38 (dd, ^4J = 2.4 Hz, ^3J = 8.3 Hz, 2H), 7.55 (t, ^3J = 5.6 Hz, 4H), 7.66 (t, ^3J = 7.8 Hz, 2H), 7.70 (s, 2H), 7.79 (s, 2H), 7.81 (s, 2H), 7.83 (m, 4H), 8.12 (d,^3J = 8.2 Hz, 4H), 8.87 (m, 8H).^{13}C NMR (100.5 MHz, 25 °C, THF-d^8): δ [ppm] = 31.9, 35.4, 36.3, 41.6, 68.7, 114.6, 115.8, 116.4, 120.4, 120.9, 121.6, 122.7, 124.2, 128.1, 129.2, 131.5, 132.1, 132.4, 135.4, 141.6, 144.8, 146.0, 146.4, 150.8, 150.9, 151.2, 157.4, 168.2. EA: calculated for $C_{72}H_{66}N_6O_8Zn \cdot 1\ CH_2Cl_2 \cdot 2H_2O$ (1330): C, 65.94; H, 5.46; N, 6.32; found: C, 65.45; H, 5.34; N, 6.40. MS (MALDI, DCTB): *m*/*z*: 1207 $[M]^+$.

Film Fabrication. The colloids have been prepared following procedures reported earlier.[2,3] Shortly, colloidal ZnO nanoparticles were prepared by hydrolyzing zinc acetate dihydrate by lithium hydroxide in ethanolic solution. A 2.19 g (0.01 mol) sample of zinc acetate dihydrate (ACS grade, 98.0%, VWR) was dissolved in 100 mL of boiling ethanol (99.98%, VWR) and cooled down to room temperature. Then, 100 mL of a lithium hydroxide (98%, VWR) solution (0.014 mol) was added dropwise to the zinc acetate solution under vigorous stirring. Immediately after synthesis, aging processes commenced with an evolving particle diameter.[3] Next, after 5 h of aging at 25 °C, the ZnO nanoparticles were washed in order to remove the still-unreacted reaction precursors and the reaction byproduct lithium acetate by repeated flocculation affected by addition of *n*-heptane (Rotisolve HPLC, Carl Roth GmbH + Co. KG). White ZnO flocculates precipitated immediately after the addition of heptane. Afterward, the supernatant containing the unwanted compounds was separated from the white ZnO precipitate by centrifugation at 3500 rpm for 15 min (Labofuge 400, Heraeus Instruments GmbH) and decantation. Finally, the ZnO flocculates were dried under nitrogen for about 5 min at room temperature in order to obtain a solid powder.

Dried ZnO particles (0.75 g) were redispersed in ethanol by adding small amounts of acetyl acetate and grinding them in a mortar. Small aliquots of a total of 2.11 g of ethyl cellulose (5−15 mPa, 10% in ethanol) and 1.64 g of ethyl cellulose (30−50 mPa, 10% in ethanol) were added to the dispersion and diluted with 3.04 g of terpineol. Then, ethanol was removed

via evaporation until a ZnO content of 20% was achieved, and the wet paste was finally homogenized by ball milling for 60 min in a Teflon-coated mill. Films (2−15 μm thick) were deposited by "doctor blading"[31] on F/SnO_2 conducting glass slides (TEC 15, Pilkington) between strips of Scotch Magic Tape (thickness of 60 μm) placed along the slide edges. The films were left to dry at 80 °C until they were transparent and then sintered at 480 °C for 30 min. Titania films were prepared similarly from a commercial TiO_2 paste (T20/SP, Solaronix SA, Switzerland), yielding comparable films.

Cell Fabrication and Characterization. Nanocrystalline metal-oxide-coated conducting glass slides with an active area of 1 cm^2 were sensitized with **1** and **2** by immersing the electrodes in a 50 μM solution of the dye in anhydrous toluene and methanol in a 9:1 ratio for up to 24 h followed by rinsing with the solvent to remove ungrafted dye. For counter electrode fabrication, uncoated conducting glass slides were cut into pieces, and holes of 1 mm^2 were drilled at the edge of the active area. A thin film of chloroplatinic acid (0.01 M H_2PtCl_6 in ethanol, Sigma-Aldrich) was spread over the conducting glass electrode, which was allowed to dry in air prior to firing at 380 °C for 20 min. Both the metal-oxide-coated conducting glass and the platinum counter electrode were then sealed together with a transparent film of Surlyn 1472 (DuPont Ltd., UK) cut as a frame around the nanocrystalline film. A solution of 0.6 M 1-methyl-3-propyl imidazolium iodide (MPII, Carl Roth GmbH + Co. KG) and 0.03 M I_2 in methoxyacetonitrile (Fluka Chemie AG) was employed as the electrolyte. The electrolyte was introduced through a hole drilled in the counter electrode and immediately sealed.

Photocurrent measurements were carried out using a Keithley Sourcemeter 2400 during illumination. A collimated light beam from an adjustable 1000 W xenon arc lamp was used for UV and Vis illumination, closely matching AM 1.5 conditions. When white light was used, a 350 nm cutoff filter was used. When recording the photoaction spectrum, a B&M Spektronik grating monochromator was introduced into the path of the excitation beam for selecting the required wavelengths. All measurements were performed after subtracting stable dark currents. The incident photon-to-current conversion efficiency (IPCE), defined as the number of electrons collected per incident photon, was determined from short circuit photocurrent measurements at different wavelengths. All experiments were performed at room temperature.

Nanosecond−Millisecond Transient Absorption Spectroscopy. For determination of transient absorption data, the samples were excited at 605 nm with pulses from a nitrogen-pumped dye laser (<1 ns pulse duration, 0.8 Hz, intensity of 0.04 mJ cm^{-2}). The laser power was adjusted to a regime low enough to not observe any laser power dependency of the transient kinetics. The optical density of the dye-sensitized films at 605 nm was 0.4. The resulting photoinduced changes in optical density were monitored by employing a 100 W tungsten lamp, with 20 nm bandwidth monochromators before and after the sample, a home-built photodiode-based detection system, and a TDS-220 Tecktronic DSO oscilloscope. UV−Vis measurements were performed after each experiment to monitor any desorption/degradation of the sensitizer dye. No changes in the UV−Vis spectra were observed for the photoelectrodes after transient absorption experiments.

Results and Discussion

Absorption Spectroscopy. It is important to establish the minimum time period necessary to completely cover the mesoporous surface due to the fact that the immersion time emerged as a decisive factor for device efficiencies.[32] Therefore, absorption spectra were recorded following different immersion intervals, that is, soaking ZnO films into solutions of either **1** or **2**. The adsorption behavior of both systems was investigated in protic solvents containing a solution of the dye since it is known to influence the efficiency of the cell.[32] In the case of **1**, we noticed that a 2 μm thick mesoporous ZnO film gives rise to a saturation behavior after approximately 100 min of immersion. This leads to conclude that the ZnO film is fully loaded with **1**. Aggregation of **1** is likely to be ruled out during the ZnO film loading since the characteristic features of **1** remain unchanged without shifts. More details with respect to the absorption kinetics of **1** or **2** were gathered by monitoring the changes in absorbance at, for example, 600 nm of 2 μm thick ZnO films until the absorbance reached a plateau. In Figure 1, the adsorption kinetics for ZnO immersion into 50 μM solutions of each dye are compared. Importantly, under identical conditions, **1** and **2** show several differences. In the case of **1**, the maximum absorbance assumes a value of 0.25 units, while for **2**, the maximum absorbance is reached at 0.2 units. A likely rationale involves the different surface areas (i.e., ZnO) necessary to accommodate one or two anchoring groups in **1** and **2**, respectively. The different structure of **1** and **2** impacts also the overall adsorption kinetics. In particular, the rate constants for adsorption were derived by means of fitting the experimental data to a pseudo-first-order Lagergren's eq 1

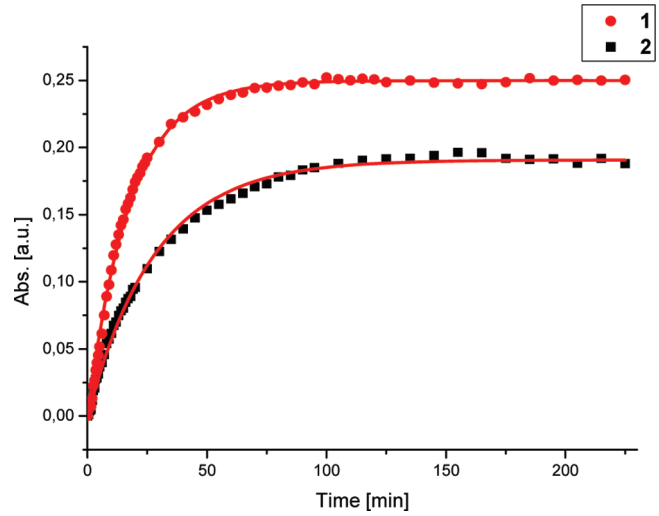

Figure 1. Absorption recorded at 600 nm of a ZnO film on glass immersed into a 50 μM solution of the porphyrin in ethanol for different time intervals. The ZnO film prior to the immersion was subtracted as the background.

$$A = A_{max}(1 - \exp(-k_{ads}t)) \quad (1)$$

where A_{max} is the maximum of absorption and k_{ads} is the rate constant for dye adsorption onto the ZnO film. The observed kinetics fits very well with a Langimur adsorption isotherm of type II. This is corroborating that only a monomolecular layer of the dye is adsorbed and that there is no interaction between neighboring molecules.

To this end, k_{ads} for **1** and **2** were calculated as 0.057 and 0.035 s^{-1}, respectively, for a dye concentration of 50 μM in solution. The somewhat slower adsorption kinetics for **2** when compared to that of **1** is understood on the basis of the fact that, despite the almost identical size of **1** and **2**, the sterically

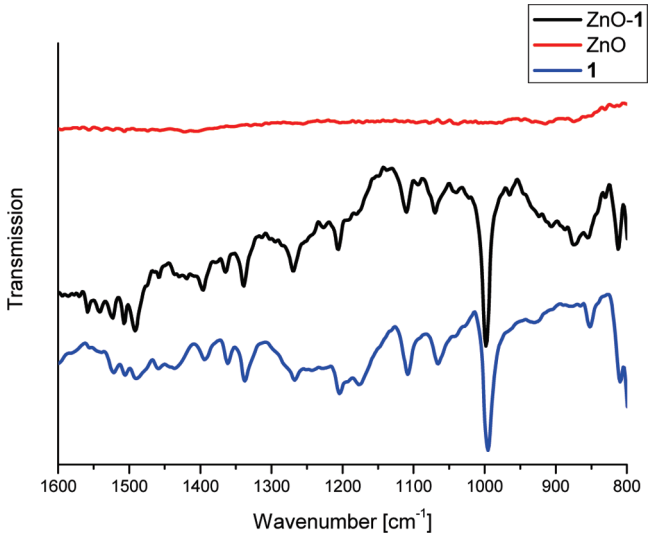

Figure 2. ATR-IR spectra in the range of 1600−800 cm^{-1} of a pristine ZnO film (red), a powder spectrum of the pure compound **1** (blue), and a ZnO film after sensitization with **1** (black).

more demanding structure of **2** slows down the diffusion into the pores of the ZnO film. Furthermore, the trans geometry in the case of **2** might block very small pores by forming bridge-like structures inside of their walls. No appreciable desorption was observed during rinsing with ethanol, toluene, or methanol. Previous work with thermogravimetric analysis coupled with mass spectroscopy (TGA-MS) experiments has corroborated the unique stability of catecholates up to about 500 °C. Carboxylic-acid-grafted acetate groups, on the other hand, were shown to desorb at about 200 °C.[2]

Attenuated Total Reflection Infrared (ATR-IR). ATR-IR studies provide valuable insights into ZnO/**1** and **2** interactions, especially into how catechol binds to the nanostructured ZnO films. In Figure 2, ATR-IR spectra of ZnO, ZnO/**1**, and just **1** are compared. Obviously, in ZnO/**1**, the aromatic ring C−C stretch vibrations are shifted, and the multiple OH bend/C−O stretch vibrations in the 1160−1310 cm^{-1} region are reduced to two peaks, 1270 and 1206 cm^{-1}. Since chelating catechol evokes a proton displacement for the phenolic groups, all of the peaks associated with OH bend vibrations are lost. Additionally, the characteristic peaks for a 1,2,4-trisubstituted benzene at 850 and 810 cm^{-1} are altered drastically. Taken the aforementioned in concert, we have successfully corroborated the attachment of the catechol functionality to ZnO.

Zinc Porphyrin (ZnP) to ZnO Charge-Transfer/Charge-Injection Kinetics. To shed light onto the injection efficiency, that is, charge transfer from photoexcited ZnP to ZnO, excited-state fluorescence lifetimes are a convenient tool. In control experiments, a mesoporous film of a wide band gap semiconductor, aluminum oxide (alumina, Al_2O_3), was employed (Figure 3). Owing to the energetically high-lying conduction band of Al_2O_3, a charge transfer from LUMO of ZnP renders thermodynamically unfeasible. In fact, the excited-state fluorescence decay of **1** on a nanostructured Al_2O_3 film is best fitted by a biexponential fitting function, which yields lifetimes of 0.31 and 1.39 ns. On the contrary, the excited-state fluorescence decay of **1** is greatly reduced when adsorbed onto a nanostructured ZnO film. Here, the lifetimes were 0.15 and 0.86 ns (Figure 3).

An additional method to analyze the excited-state fluorescence decay is applying a modified Kohlrausch−Williams−Watts (KKW) fitting function[33]

$$\text{Intensity}(t) \propto \exp[-(t/\tau)^{\alpha}] \qquad (2)$$

With respect to the inhomogeneous broadening of the energetics, application of the KWW fitting function becomes a necessity. Accordingly, we estimated that charge transfer/charge injection for **1** occurs in less than 100 ps. As Figure 4 documents, **2** gives rise to very similar kinetics at least on the time scale of 100−1000 ps. These values are in excellent agreement with values obtained for porphyrins grafted via carboxylic acid linkers onto TiO_2, underlining the good match between the catechol anchoring group and ZnO.[34] This suggests that the difference between face-to-edge/orthogonal and face-to-face/parallel orientations imposes no major impact on the charge-transfer/charge-injection kinetics. Further support for this notion came from steady-state fluorescence measurements revealing that the charge-transfer/charge-injection efficiency exceeds 90% for **1** and **2**. Remarkable is the efficiency of this process despite the long, not fully conjugated anchoring groups.

ZnP to ZnO Charge Recombination Kinetics. Transient absorption spectroscopy emerged as a powerful tool to provide meaningful insight into the recombination dynamics. In particular, the product of charge transfer/charge injection, that is, the one-electron oxidized ZnP radical cation, is monitored in the absence of any electrolyte (i.e., I_3^-/I^-) capable of reducing the ZnP radical cation. This leaves charge recombination between the ZnP radical cation and the newly injected conduction band electron in ZnO as the only feasible pathway. It was shown in previous work that the recombination dynamics in TiO_2-based DSSCs depend strongly on the applied bias and are influenced by high laser powers.[35] Therefore, all experiments were conducted utilizing a laser power well below the threshold of influencing the kinetics. Figure 5 illustrates the recombination dynamics between the conduction band electron of ZnO, on one hand, and the one-electron oxidized forms of **1** or **2**, on the other hand, at 680 nm, which coincides with the maximum absorption of the ZnP radical cation signature.[36] Within the time resolution of our apparatus, we found one major decay component for ZnO/**1** and ZnO/**2**. The decays are reasonably fitted by eq 2 due to an appreciable energetic broadening that relates to trapping and/or detrapping charges. Our kinetic analyses yield lifetimes of 116 and 123 μs for ZnO/**1** and

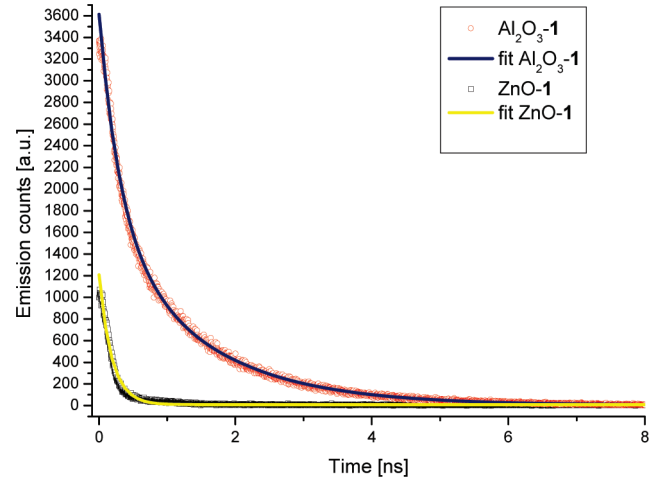

Figure 3. Time-correlated single-photon counting measurements for the emission (at 605 nm) of **1** grafted onto a Al_2O_3 film on glass (red circles) and of **1** grafted onto a ZnO film on glass (black squares) adjusted to the same optical density at the exitation wavelength of 405 nm. The decays were fitted and are plotted for **1** on Al_2O_3 (blue line) as well as for **1** on ZnO (yellow line).

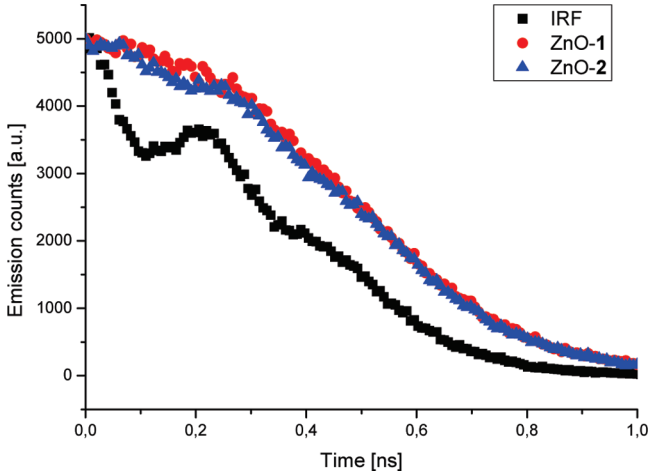

Figure 4. Time-correlated single-photon counting measurements of the emission at 600 nm of **1** (red circles) and **2** (blue triangles), each with the same optical density, on ZnO films after excitation at 405 nm. The instrument response function is also depicted (black squares).

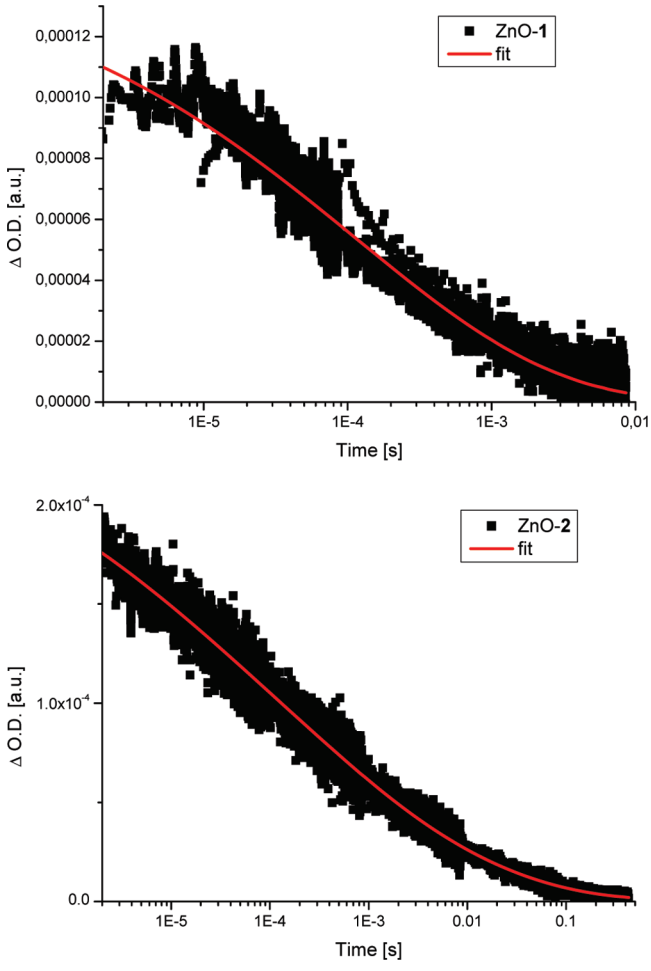

Figure 5. Transient absorption spectroscopy of the electron recombination dynamics for a 6 μm thick dye-sensitized ZnO film. The probes were excited by the emission at 605 nm of a Rhodamine 6G dye pumped at 337 nm by a nitrogen laser, and the probe wavelength was fixed at 680 nm.

ZnO/**2**, respectively. Interestingly, there is an invariance of the charge recombination kinetics underlining the point that the orientation of the porphyrin relative to the metal oxide might not play a vital role in the charge-transfer process. The regeneration dynamics for this film are shown in Figure 6.

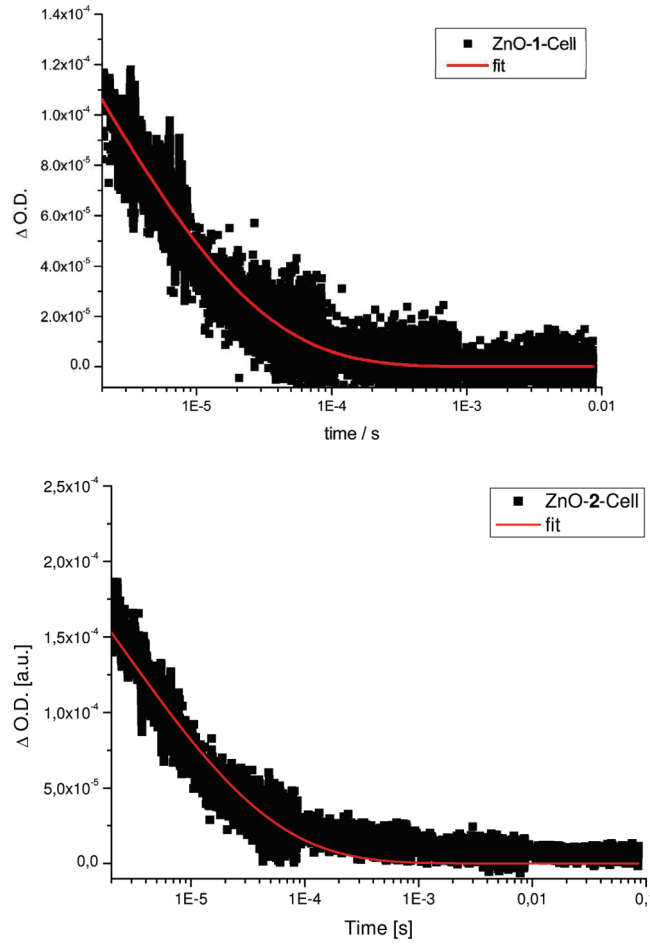

Figure 6. Transient absorption spectroscopy of the dye regeneration dynamics for a 6 μm thick dye-sensitized ZnO film. The probes were excited by the emission at 605 nm of a Rhodamine 6G dye pumped at 337 nm by a nitrogen laser, and the probe wavelength was fixed at 680 nm.

Decisive are reference measurements with nanostructured TiO_2 films rather than ZnO (see Supporting Information). In the absence of the I_3^-/I^- redox-active electrolyte, which assisted in monitoring the intrinsic lifetime of the ZnP radical cation/conduction band electron in TiO_2, a lifetime (i.e., 7.72 ms) was found that exceeds that seen for the analogous ZnO system (i.e., 116 μs). This important observation is likely to relate to the different electron densities of TiO_2 and ZnO. In fact, step chronoamperometry (see Supporting Information) provides values of the ZnO electron densities that are up to 1 order of magnitude higher than the corresponding values for TiO_2. Similar results have already been described in the literature, and the findings are transferable to our system despite following a different synthesis route and employing completely different sensitizers.[37] Implicit are dramatic consequences for the charge recombination, which scales with the electron density. In fact, the different recombination lifetimes, when contrasting ZnO and TiO_2, reflect this trend.

ZnP to Electrolyte Charge Shift Kinetics. In stark contrast to the aforementioned, the charge shift dynamics between the one-electron oxidized forms of **1** or **2** and the I_3^-/I^- redox-active electrolyte were determined in the presence rather than in the absence of the latter. To this end, a complete cell, ZnO, **1** or **2**, and, I_3^-/I^-, was employed. Notably, we expected, in close agreement with previous investigations, the decay dynamics to change from a strictly monoexponential first-order process to a biexponential second-order process.[38,39] Importantly, charge

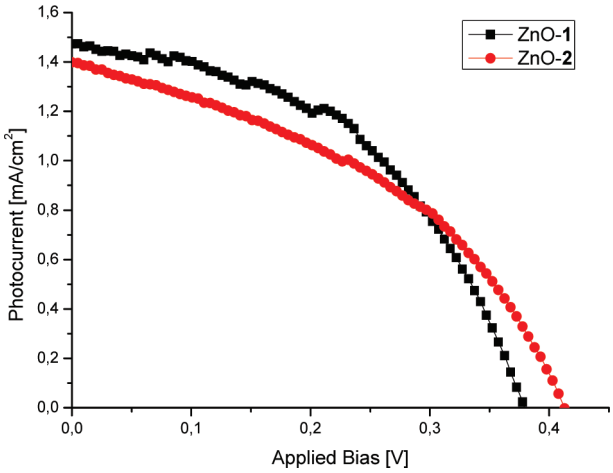

Figure 7. Current−voltage characteristics for DSSC devices under 100 mW/cm^2 of AM 1.5 illumination.

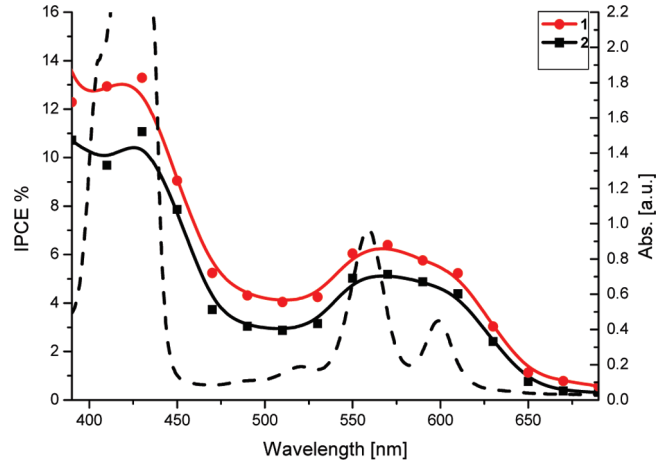

Figure 8. Wavelength-dependent incident photon-to-current efficiencies of DSSC devices sensitized with **1** and **2**. The absorption spectrum of **1** on ZnO is shown as a dashed line.

recombination dominates in the absence of I_3^-/I^-, while the presence of I_3^-/I^- results in a charge shift reaction yielding a reinstated ZnP ground state and the formation of further byproduct. Previous work has demonstrated that, quite often, a second phase is observed when the electrolyte is present. In fact, this signal arises from a slower formation of byproduct as a result of regenerating the ground state of the sensitizer by subsequent electron transfer from the I_3/I^- electrolyte.[39] Nevertheless, the formation of any byproduct could not be confirmed kinetically. A likely rationale for the absence of the latter is the overall weak signals during measurements with a complete cell. Thus, the process in the presence of I_3^-/I^- is attributed exclusively to a concentration-dependent regeneration of the ZnP radical cation as a means to react with the electrolyte. As the I_3^-/I^- concentration increases, the charge shift reaction starts to compete with the charge recombination. For example, at a time delay of 2 μs and a concentration of 0.03 M I_2 and 0.6 M I^-, the ZnP radical cation transient has completely disappeared. In other words, under standard operation conditions, the charge shift reaction outperforms the intrinsic charge recombination reaction by two orders of magnitude. On account of the face-to-face/parallel versus face-to-edge/orthogonal orientations, no appreciable changes were discernible between ZnO/**1** and ZnO/**2**, suggesting that the rate-determining step is the interaction with ZnP rather than any impact imposed by the anchoring groups.

Finally, the charge shift kinetics were investigated with a complete cell based on nanostructured TiO_2 films. In the case of TiO_2/**1**, charge shift kinetics were established to be 2.32 μs, which resemble those of ZnO/**1**, 1.80 μs. This leads us to rule out a substrate-selective step, namely, ZnO- versus TiO_2-dependent regeneration of ZnP as a bottleneck in the overall device performance. Another, even more important, conclusion is concerned with relative kinetics of charge recombination and charge shift. Our experiments attest that the charge recombination imposes no limitation on the charge shift and is kinetically nonrelevant even if the kinetic difference between the two steps is, like in the case of ZnO, as small as 2 orders of magnitude.

Current−Voltage Characteristics. The device performance was tested for cells based on nanostructured ZnO films sensitized with **1** or **2**. At first glance, the current−voltage characteristics (see Figure 7) are in close agreement with ZnP-sensitized solar cells.[38] In particular, the following features emerge: an open circuit voltage of around 0.4 V and a short circuit current of around 1.5 mA/cm^2 under full one sun illumination. A closer analysis sheds light onto a few minor differences between the nanostructured ZnO films sensitized with either **1** or **2**. The short circuit current for **1** (i.e., 1.47 mA/cm^2) is, for example, slightly higher than that for **2** (i.e., 1.40 mA/cm^2). These values are comparable to short circuit currents obtained upon sensitizing metal oxides with porphyrins.[34] This observation tracks the trend seen in the optical absorptions of ZnO/**1** are higher than those in ZnO/**2** with optical densities at 552 nm of 0.68 and 0.55, respectively. Here, a slightly higher ZnP uptake due to less spatial requirements might affect the short circuit current. The open circuit voltage is, however, higher for **2** (i.e., 0.42 V) than that for **1** (i.e., 0.38 V). The tied face-to-face/parallel orientation of ZnO and **2** is likely to perturb the electronic structure of ZnP and to render the ZnP oxidation thermodynamically harder.[27,36] The shifted ZnP oxidation, on the other hand, widens the energy gap between the ZnP/ZnP radical cation and the I_3^-/I^- couples and, in turn, increases the open circuit voltage. This is also reflected in the power conversion efficiencies, which are 0.27% for **1** and 0.23% for **2**.

Following the same procedure, TiO_2/**1** and TiO_2/**2** solar cells were fabricated and tested. When contrasting TiO_2/**2** with ZnO/**2**, the overall ZnP loading was greatly reduced in the former case. On the contrary, the ZnP loading in TiO_2/**1** and ZnO/**1** was comparable. It is interesting to note that the use of either **1** or **2** results in essentially the same open circuit voltage with, however, different short circuit current. The latter, namely, the lower short circuit currents in TiO_2/**1** and TiO_2/**2**, is attributed to lower coverage of **1** or **2**. At the present stage, it is, however, unclear to us why the nanostructured TiO_2 films feature lower coverage. Smaller pore sizes in the case of TiO_2 might be one of the reasonable explanations as it would correlate with a diffusion of **2** into the pores that is hindered.

Incident Photon-to-Current Conversion. The IPCE spectra, as they are depicted in Figure 8, illustrate through features resembling the ZnP ground,state absorption that indeed the charge transfer/charge injection evolves from photoexcitation of ZnP to ZnO. Nevertheless, it is noteworthy that the yields of charge transfer/charge injection in the region corresponding to the Q-band absorption (i.e., 500−650 nm) is somewhat stronger than that in the Soret band region (i.e., 400−450 nm) when just compared to the relative absorbances in the ground state. Interesting is the appreciable photocurrent generation in the spectral region that bridges the Soret and Q-band absorption, which is due to spectral broadening of ZnP on ZnO. Furthermore, the photosensitization seems to be more efficient when

comparing the corresponding ground-state absorptions in the Q-band region than that in the Soret band region. Such observation relates to the intrinsically fast interconversion of higher-lying singlet excited states into the first singlet excited state; this happens on the order of 1−2 ps.[40] In this regard, we hypothesize that such "high-energy" electrons are rapidly downconverted without, however, contributing to the overall photocurrent conversion efficiency.

Finally, the different cell performances should be compared. TiO_2/**1** performs slightly better than ZnO/**1**, while the performances of TiO_2/**2** and ZnO/**2** are generally poor. In line with the absorption characteristics of TiO_2/**2** and ZnO/**2**, an incomplete grafting of **2** to TiO_2 or ZnO might be responsible for this trend. Of particular interest is the absence of charge transfer/charge injection for TiO_2/**2** in the Q-band region. Here, an unfavorable geometry relative to/electronic coupling to the TiO_2 conduction bands might augment effects that stem from the low coverage.

Conclusions

The current investigation sheds light onto implementing two different ZnP's with either face-to-face/parallel or face-to-edge/orthogonal orientations relative to nanostructured ZnO (i.e., ZnO/**1** and ZnO/**2**) and/or TiO_2 (i.e., TiO_2/**1** and TiO_2/**2**) surfaces. A detailed cell characterization combined with a complete investigation on kinetics and light-to-energy conversion performances has identified the following bottlenecks for achieving an optimum DSSC configuration. First, the relative orientation of ZnP relative to ZnO or TiO_2 is a decisive factor since it affects the electronic coupling as a means to mediate charges across the various interfaces. Second, choosing the proper pore size of nanostructured ZnO or TiO_2 films needs consideration to balance diffusion of ZnP for an efficient grafting/loading, on one hand, and diffusion of injected charges within ZnO or TiO_2 to the charge-collecting electrodes, on the other hand. Our studies corroborate also that nanostructured ZnO films bear great incentives for the development of emerging device technology.

Acknowledgment. The authors gratefully acknowledge the funding of the German Research Council (DFG), which, within the framework of its "Excellence Initiative", supports the Cluster of Excellence "Engineering of Advanced Materials" (www.eam.uni-erlangen.de) at the University of Erlangen−Nuremberg. E.P. thanks the MICINN for the Project CONSOLIDER HOPE 2007-00007, ICIQ and ICREA for financial support.

Supporting Information Available: Electron density measurements, transient absorption spectroscopy, and current−voltage characteristics. This material is available free of charge via the Internet at http://pubs.acs.org.

References and Notes

(1) Law, M.; Greene, L. E.; Johnson, J. C.; Saykally, R.; Yang, P. *Nat. Mater.* **2005**, *4*, 455.
(2) Marczak, R.; Werner, F.; Gnichwitz, J. F.; Hirsch, A.; Guldi, D. M.; Peukert, W. *J. Phys. Chem. C* **2009**, *113*, 4669.
(3) Marczak, R.; Segets, D.; Voigt, M.; Peukert, W. *Adv. Powder Technol.* **2010**, *1*, 41.
(4) Kar, S.; Dev, A.; Chaudhuri, S. *J. Phys. Chem. B* **2006**, *110*, 17848.
(5) Baruah, S.; Dutta, J. *Sci. Technol. Adv. Mater.* **2009**, *10*, 1.
(6) Wang, Z. L. *J. Phys.: Condens. Matter.* **2004**, *16*, R829.
(7) Ghoshal, T.; Kar, S.; Chaudhuri, S. *J. Cryst. Growth* **2006**, *293*, 438.
(8) Solbrand, A.; Lindstrom, H.; Rensmo, H.; Hagfeldt, A.; Lindquist, S. E.; Sodergren, S. *J. Phys. Chem. B* **1997**, *101*, 2514.
(9) Solbrand, A.; Keis, K.; Södergren, S.; Lindström, H.; Lindquist, S. E.; Hagfeldt, A. *Sol. Energy Mater. Sol. Cells* **2000**, *60*, 181.
(10) Grätzel, M. *J. Photochem. Photobiol. C* **2003**, 145.
(11) O'Regan, B.; Grätzel, M. *Nature* **1991**, *353*, 737.
(12) M. Quintana; Edvinsson, T.; Hagfeldt, A.; Boschloo, G. *J. Phys. Chem. C* **2007**, *111*, 1035.
(13) Haque, S. A.; Palomares, E.; Green, B. M.; Alex, N. M.; Hirata, H.; Klug, D. R.; Durrant, J. R. *J. Am. Chem. Soc.* **2005**, *110*, 3456.
(14) Keis, K.; Lindgren, J.; Lindquist, S. E.; Hagfeldt, A. *Langmuir* **2000**, *16*, 4688.
(15) Kadish, K. M.; Smith, K. M.; Guilard, R. *The Porphyrin Handbook*; Academic Press: New York, 1999.
(16) Hervás, M.; Navarro, J. A.; Rosa, M. A. D. l. *Acc. Chem. Res.* **2003**, *36*, 798.
(17) Kay, A.; Grätzel, M. *J. Phys. Chem.* **1993**, *97*, 6272.
(18) Wang, Q.; Campbell, W. M.; Bonfantani, E. E.; Jolley, K. W.; Officer, D. L.; Walsh, P. J.; Gordon, K.; Humphry-Baker, R.; Nazeeruddin, M. K.; Grätzel, M. *J. Phys. Chem. B* **2005**, *109*, 15397.
(19) Campbell, W. M.; Jolley, K. W.; Wagner, P.; Wagner, K.; Walsh, P. J.; Gordon, K. C.; Schmidt-Mende, L.; Nazeeruddin, M. K.; Wang, Q.; Grätzel, M.; Officer, D. L. *J. Phys. Chem. C* **2007**, *111*, 11760.
(20) Nazeeruddin, M. K.; Humphry-Baker, R.; Officer, D. L.; Campbell, W. M.; Burrell, A. K.; Grätzel, M. *Langmuir* **2004**, *20*, 6514.
(21) Clifford, J. N.; Palomares, E.; Nazeeruddin, M. K.; Grätzel, M.; Nelson, J.; Li, X.; Long, N. J.; Durrant, J. R. *J. Am. Chem. Soc.* **2004**, *126*, 5225.
(22) Palomares, E.; Martinez-Diaz, M. V.; Haque, S. A.; Torres, T.; Durrant, J. R. *Chem. Commun.* **2004**, *18*, 2112.
(23) Durrant, J. R.; Haque, S. A.; Palomares, E. *Coord. Chem. Rev.* **2004**, *248*, 1247.
(24) Galoppini, E.; Guo, W.; Qu, P.; Meyer, G. J. *J. Am. Chem. Soc.* **2001**, *123*, 4342.
(25) Galoppini, E.; Guo, W.; Zhang, W.; Hoertz, P.; Qu, P.; Meyer, G. J. *J. Am. Chem. Soc.* **2002**, *124*, 7801.
(26) Clark, C. C.; Meyer, G. J.; Wei, Q.; Galoppini, E. *J. Phys. Chem. B* **2006**, *110*, 11044.
(27) Rochford, J.; Chu, D.; Hagfeldt, A.; Galoppini, E. *J. Am. Chem. Soc.* **2007**, *129*, 4655.
(28) Verma, S.; Kar, P.; Das, A.; Palit, D. K.; Ghosh, H. G. *J. Phys. Chem. C* **2008**, 112.
(29) Ramakrishna, G.; Verma, S.; Jose, D. A.; Krishna Kumar, D.; Das, A.; Palit, D. K.; Ghosh, H. N. *J. Phys. Chem. B* **2006**, *110*, 9012.
(30) Perrin, D. D.; Amarego, W. L. F. *Purification of Laboratory Chemicals*, 3rd ed; Pergamon Press: Oxford, U.K., 1988.
(31) Ito, S. *J. Mater. Chem.* **2004**, *14*, 385.
(32) Imahori, H.; Hayashi, S.; Hayashi, H.; Oguro, A.; Eu, S.; Umeyama, T.; Matano, Y. *J. Phys. Chem. C* **2009**, *113*, 18406.
(33) Koops, S.; Durrant, J. R. *Inorg. Chim. Acta* **2008**, *361*, 663.
(34) Dos Santos, T.; Morandeira, A.; Koops, S.; Mozer, A. J.; Tsekouras, G.; Dong, Y.; Wagner, P.; Wallace, G.; Earles, J. C.; Gordon, K. C.; Officer, D.; Durrant, J. R. *J. Phys. Chem. C* **2010**, *114*, 3276.
(35) Haque, S. A.; Tachibana, Y.; Willis, R. L.; Moser, J. E.; Grätzel, M.; Klug, D. R.; Durrant, J. R. *J. Phys. Chem. B* **2000**, *104*, 358.
(36) Guldi, D. M.; Luo, C.; Prato, M.; Troisi, A.; Zerbetto, F.; Scheloske, M.; Dietel, E.; Bauer, W.; Hirsch, A. *J. Am. Chem. Soc.* **2001**, *123*, 9166.
(37) Willis, R. L.; Olson, C.; O'Regan, B.; Lutz, T.; Nelson, J.; Durrant, J. R. *J. Phys. Chem. B* **2002**, *106*, 7605.
(38) Forneli, A.; Planells, M.; Sarmentero, M. A.; Martinez-Ferrero, E.; O'Regan, B. C.; Ballester, P.; Palomares, E. *J. Mater. Chem.* **2008**, *18*, 1652.
(39) Montanari, I.; Nelson, J.; Durrant, J. R. *J. Phys. Chem. B* **2002**, *106*, 12203.
(40) Mataga, N.; Chosrowjan, H.; Taniguchi, S.; Shibata, Y.; Yoshida, N.; Osuka, A.; Kikuzawa, T.; Okada, T. *J. Phys. Chem. A* **2002**, *106*, 12191.

JP102737A